



## ENVIRONMENTAL STUDIES

# Radar remote sensing reveals potential underestimation of rainfall erosivity at the global scale

Qiang Dai<sup>1</sup>, Jingxuan Zhu<sup>1,5</sup>, Guonian Lv<sup>1\*</sup>, Latif Kalin<sup>2</sup>, Yuanzhi Yao<sup>2,3\*</sup>, Jun Zhang<sup>1,4</sup>, Dawei Han<sup>5</sup>

Rainfall kinetic energy (RKE) constitutes one of the most critical factors that drive rainfall erosivity on surface soil. Direct measurements of RKE are limited, relying instead on the empirical relations between kinetic energy and rainfall intensity (*KE-I* relation), which have not been well regionalized for data-scarce regions. Here, we present the first global rainfall microphysics-based RKE ( $RKE_{MPH}$ ) flux retrieved from radar reflectivity at different frequencies. The results suggest that  $RKE_{MPH}$  flux outperforms the RKE estimates derived from a widely used empirical *KE-I* relation ( $RKE_{KE-I}$ ) validated using ground disdrometers. We found a potentially widespread underestimation of  $RKE_{KE-I}$ , which is especially prominent in some low-income countries with ~20% underestimation of RKE and the resultant rainfall erosivity. Given the evidence that these countries are subject to greater rainfall-induced soil erosion, these underestimations would mislead conservation practices for sustainable development of terrestrial ecosystems.

## INTRODUCTION

Soil erosion is a denudation or wearing process that drives the splashing of tiny particles from the upper layers of the soil mass. Accelerated soil erosion, primarily driven by anthropogenic disturbances, has detrimental impacts on the terrestrial ecosystem. Improving the accuracy of soil erosion assessment models at the regional and global scales is critical to ensure the sustainability of conservation practices (1–4). Rainfall-induced soil erosion, which is initiated by the kinetic energy of raindrop motion (5), accounts for most of the global soil loss (6), yet the mechanistic representation associated with the rainfall energy in the current soil erosion models remains largely uncertain.

The full dynamics of rainfall kinetic energy (hereinafter RKE) can be quantified using raindrop microphysics, which includes physical parameters for raindrop size and falling velocity. However, quantification of the physical parameters and the associated observations for raindrop microphysics (velocity, size, and morphology) at large spatial scales has been a long-term challenge. It requires a better mechanistic understanding, considerable labor, and a dense observational network with expensive equipment such as disdrometers (instruments capable of measuring raindrop size and falling velocity) (7, 8). To simplify the calculation, substantial efforts have been devoted to the development of empirical relations between RKE flux and rainfall intensity (also known as *KE-I* relation), represented in linear (9, 10), polynomial (11), exponential (12, 13), logarithmic (14, 15), and power-law (8) functions. However, such empirical relationships are regionally limited under specific climate conditions and precipitation microphysics, resulting in great uncertainties and poor spatial and temporal predictability of RKE and rainfall erosivity in many parts of the world (16).

This uncertainty is possible to enhance under the fact of climate change. It has been observed that winter precipitation around the world is shifting from snow to rainfall (17), which has much larger kinetic energy with the same amount of precipitation, particularly in regions with a more maritime climate (18). In general, raindrop size and velocity are sensitive to air temperature, which would result in notable changes in RKE fluxes in the context of a warmer climate (6). This has prompted the scientific community to seek for previously unidentified technologies to monitor raindrop microphysics and the associated RKE dynamics at large scales (19, 20).

In recent years, ground- and space-based radars have shown promising capabilities for monitoring RKE fluxes (20–22). Compared to the ground dual-polarization radars that are available in limited areas (23), the space-borne dual-frequency precipitation radar (DPR) radar contains Ku band (13.6 GHz) and Ka band (35.5 GHz) on the Global Precipitation Measurement (GPM) core satellite. It allows the global monitoring of the spatial distribution of hydrometeors in three dimensions, providing new insights into the overall assessment of global rainfall erosivity estimates.

Following the recent advancement of the DPR radar products, we provide the first global-level estimation of rainfall microphysics-based RKE ( $RKE_{MPH}$ ) flux spanning from 2015 to 2019 at a spatial resolution of  $0.1^\circ \times 0.1^\circ$  between  $60^\circ\text{N}$  and  $60^\circ\text{S}$ , covering ~87% of the Earth's land surface ( $\sim 1.18 \times 10^8 \text{ km}^2$ ). We excluded the boreal region of the North Hemisphere and Antarctica, assuming that the  $RKE_{MPH}$  is negligible in these areas. The raindrop microphysical characteristics are measured and considered in the energy estimation (detailed descriptions of the workflow of the proposed rainfall erosivity modeling can be found in fig. S1). The relationship between  $RKE_{MPH}$  and rainfall intensity within and between different years and regions is investigated. We evaluated the daily rainfall and raindrop microphysics based on radar remote sensing against meteorological data with 4,602,282 daily records and disdrometer data distributed around the world, which showed an overall realistic representation of the observed RKE (Materials and Methods and figs. S2 to S8). Our  $RKE_{MPH}$  products and the resultant rainfall erosivity are then compared with the traditional

<sup>1</sup>Key Laboratory of VGE of Ministry of Education, Nanjing Normal University, Nanjing, China. <sup>2</sup>College of Forestry, Wildlife and Environment, Auburn University, Auburn, AL, USA. <sup>3</sup>School of Geographic Science, East China Normal University, Shanghai, China. <sup>4</sup>Department of Hydrology and Atmospheric Sciences, The University of Arizona, Tucson, USA. <sup>5</sup>Department of Civil Engineering, University of Bristol, Bristol, UK.

\*Corresponding author. Email: gnlu@njnu.edu.cn (G.L.); yaoyuanzhi@auburn.edu (Y.Y.)

estimates derived from a global  $KE-I$  relation ( $RKE_{KE-I}$ ), which was incorporated into the Revised Universal Soil Loss Equation, version 2 (RUSLE2) model (24) and has been widely accepted for global and regional applications. An in-depth regional analysis of RKE and rainfall erosivity was conducted, unearthing a previously overlooked caveat of the global rainfall erosivity assessments.

## RESULTS

### Global spatial and temporal patterns of RKE flux

Our results indicate that the annual  $RKE_{MPH}$  reaching the Earth's land surface during the 2015–2019 period was  $1.36 \pm 0.30 \times 10^{18}$  J year<sup>-1</sup> (the SD indicates the interannual variation), and the flux was  $116.6 \pm 2.6$  MJ ha<sup>-1</sup> year<sup>-1</sup> between 60°S and 0°N. The  $RKE_{MPH}$  fluxes show remarkable spatial heterogeneity, with the area that has  $RKE_{MPH}$  flux greater than 322 MJ ha<sup>-1</sup> year<sup>-1</sup> (~16.75% of the global  $RKE_{MPH}$  flux), occupying about 5% of the study area, as depicted in Fig. 1A. The largest  $RKE_{MPH}$  fluxes were observed in tropical regions, more specifically, the rainforests in the Amazon basin of South America, Central Africa, and Southeast Asia (Fig. 1A), with the magnitude of fluxes in the range of ~200 to 500 MJ ha<sup>-1</sup> year<sup>-1</sup>. On the other hand, as expected, arid regions, such as the Sahara Desert in North Africa, western Asia, and Australia in Oceania, had extremely low-level RKE fluxes (lower than 20 MJ ha<sup>-1</sup> year<sup>-1</sup>) (Fig. 1A). At the continental level, the  $RKE_{MPH}$  flux in Europe does not exhibit notable spatial variation, although its magnitude is comparable to those in Asia, North America, and Africa (Fig. 1B). There is no substantial difference between the annual  $RKE_{MPH}$  fluxes during the 5 years at the continental scale, except for Oceania, where a decreasing trend is observed (Fig. 1B).

The global  $RKE_{MPH}$  fluxes, in line with the monthly variations in precipitation, show large seasonal variations (Fig. 2). In the Northern Hemisphere equatorward of 15°N, the greater amounts of

precipitation (300 to 500 mm) and  $RKE_{MPH}$  fluxes (25 to 40 MJ ha<sup>-1</sup> year<sup>-1</sup>) occur from May to September, while the counterpart of the Southern Tropic (from 0°S to 20°S) has comparable elevated values from October to April. Precipitation and  $RKE_{MPH}$  flux systematically decreased northward from 15°N to 30°N, followed by a slight increase when moving further northward (from 30°N to 60°N), primarily driven by the vertical atmospheric circulation of Hadley and Ferrel cells (Fig. 2). Similar latitudinal and seasonal patterns in the Southern Hemisphere can be explained by the aforementioned vertical atmospheric circulations. Collectively, the average  $RKE_{MPH}$  flux in the tropics (from 23°S to 23°N) is around three times greater than that in the temperate regions (north of 23°N or south of 23°S). Furthermore, we observed an obvious seasonal variation of the  $RKE_{MPH}$  flux in the tropics. For example, in the northern part of South America (near the equator), the  $RKE_{MPH}$  flux in September is less than half of that in March. However, a relatively stable aperiodic  $RKE_{MPH}$  flux is discernable at the temperate regions of both the Northern and Southern Hemispheres.

Figure 2 shows that there is a strong synchronous temporal pattern between the  $RKE_{MPH}$  fluxes and precipitation at the monthly scale, which is also confirmed by the high correlations between the  $RKE_{MPH}$  fluxes and precipitation at different months with coefficient of determination ( $R^2$ ) values that are mostly higher than 0.95 (fig. S9). This has been observed in the previously documented site-level experiments (8, 14, 19, 20). Moreover, we used rainfall energy density (RED) index, represented as the ratio of annual  $RKE_{MPH}$  flux to annual precipitation, to investigate the spatial inconsistency between them (Supplementary Text and fig. S10). Specifically, we found that  $RKE_{MPH}$  flux does not always follow the same spatial pattern as rainfall, where we found the lower RED in tropical forests that receive high annual rainfall and high RED in the central United States with relatively low annual rainfall (fig. S10).

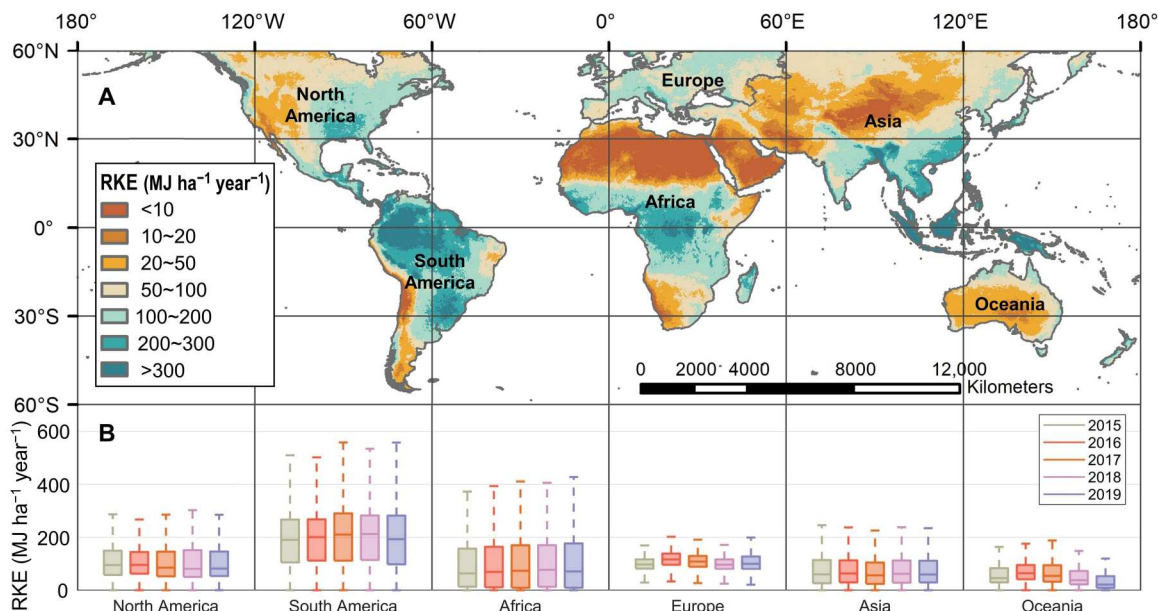


**Fig. 1. The spatial pattern of  $RKE_{MPH}$  flux and continental statistics.** (A) Five-year averaged global  $RKE_{MPH}$  fluxes estimated by remote sensing monitoring (GPM-L2 DPR and GPM-L3 IMERG). (B) Boxplots for the spatially averaged  $RKE_{MPH}$  fluxes of the six major continents. Note that the outliers are presented in Fig. 4.

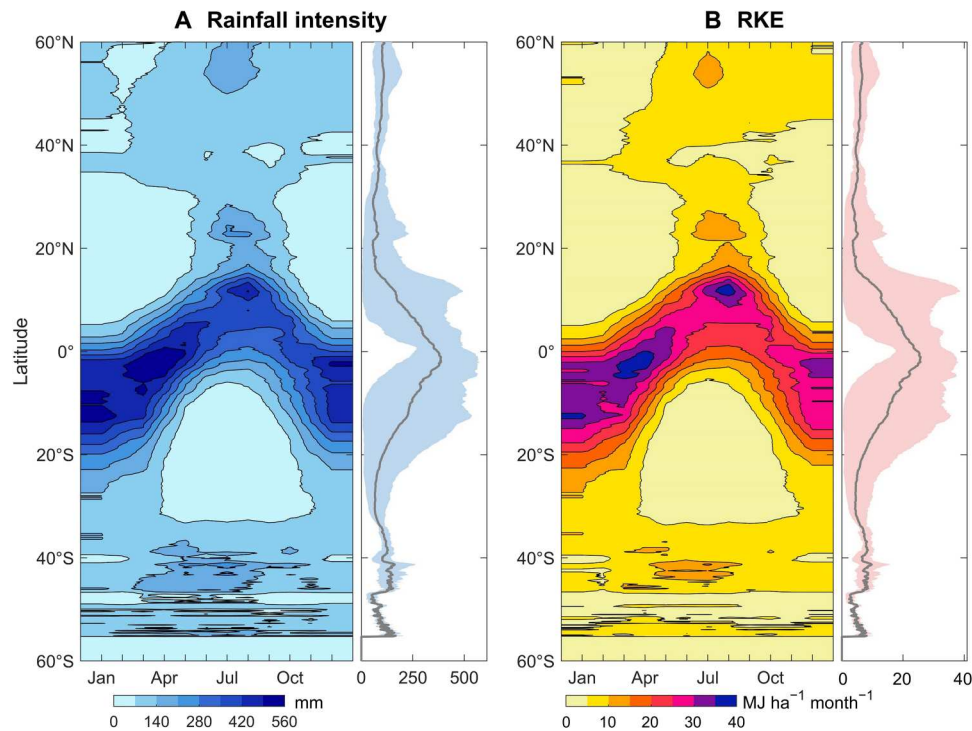


**Fig. 2. The latitudinal representation of changes in rainfall intensity and  $RKE_{MPH}$  flux.** (A) The monthly rainfall intensity averaged over the period 2015–2019. (B) The monthly  $RKE_{MPH}$  flux averaged over the period 2015–2019. The bands in the figures that are on the right side of the maps represent the 5-year average monthly variations.

### Comparison of RKEs using rainfall microphysics and $KE-I$ relations

Following the evidence of the notable spatial inconsistency between RKE fluxes and annual precipitation, we compared the rainfall  $RKE_{MPH}$  flux derived from radar measurement against the RKE flux based on a global  $KE-I$  relation ( $RKE_{KE-I}$ ). At the site level, we were able to validate our rainfall and raindrop microphysics datasets using global rain gauges and disdrometers (figs. S2 to S8 and table S1). The results showed that, of the 8557 available gauges, 71.59% of the sites had absolute relative bias values less than 0.3 (fig. S2). The fitting curves of  $KE-I$  relations derived from GPM DPR observation for  $RKE_{MPH}$  were also found to have an overall realistic representation of the observed characteristics, with a Pearson correlation coefficient greater than 0.5 and mean absolute error (MAE) less than  $5 \text{ J m}^{-2} \text{ mm}^{-1}$ , which is better than the empirical formula used in the RUSLE2 model for  $RKE_{KE-I}$ , as shown in fig. S4. Zooming in on individual stations, we found that the fit curves of  $RKE_{MPH}$  are very close to the ones derived from drop size distribution (DSD) data from disdrometers, while the ones of  $RKE_{KE-I}$  show obvious shifting patterns (fig. S5). Collectively, those for  $RKE_{MPH}$  are expected to outperform the  $KE-I$  relationship for  $RKE_{KE-I}$  with a higher Pearson correlation coefficient ( $\sim 0.57$  higher) and lower MAE ( $\sim 5.58 \text{ J m}^{-2} \text{ mm}^{-1}$  lower) (table S1).

We quantified the percent bias of RKE ( $PBIAS_{RKE}$ ) for each grid cell by comparing  $RKE_{MPH}$  and  $RKE_{KE-I}$ . The global distribution and the averaged statistics at the country and continental levels are presented in Fig. 3. A positive  $PBIAS_{RKE}$  represents an overestimation of RKE flux, and a negative  $PBIAS_{RKE}$  denotes an underestimation of RKE flux (Fig. 3). We found a globally widespread underestimation of RKE flux, with the lowest  $PBIAS_{RKE}$  ( $-14.5\%$ )

found in Africa, followed by Europe ( $-12.5\%$ ), North America ( $-10.9\%$ ), Oceania ( $-10.36\%$ ), Asia ( $-8.12\%$ ), and South America ( $-6.17\%$ ) (Fig. 3, A and B). Specifically, we identified the hot spot of RKE flux underestimation in central Africa, central Asia, and southern Asia, with the  $PBIAS_{RKE}$  reaching  $-30\%$  (Fig. 3A). For large countries with spatial heterogeneity such as the United States, the underestimation is mainly distributed in the Midwest and Southwest (such as Nebraska, Kansas, and New Mexico). We averaged the  $PBIAS_{RKE}$  for each country and organized the countries into underestimating and overestimation groups with four income levels (Fig. 3C). We performed an unequal sample size  $t$  test for each of the two income levels to determine whether the  $PBIAS_{RKE}$  of two levels differed from each other. We found that, in the underestimation group, the  $PBIAS_{RKE}$  values of the low-income level are significantly lower than that of the other three levels ( $P < 0.05$  in  $t$  test) (fig. S11A). None of the low-income countries were classified in the overestimation group, and none of the other income level pairs show a significant difference (Fig. 3C and fig. S11B).

The extremely large RKE fluxes associated with extreme events, i.e., high outliers in the continental boxplots (see Fig. 1B), were largely underestimated in tropical regions (Fig. 4). The magnitude of the averaged outliers for  $RKE_{MPH}$  flux and  $RKE_{KE-I}$  flux in high-latitude countries, such as the United States, Canada, Europe, and Australia, was mostly less than  $200 \text{ MJ ha}^{-1} \text{ year}^{-1}$ , which is relatively lower than that in the tropical regions (the ones distributed in tropical regions shown in Fig. 4, A and B). The countries with extreme events for  $RKE_{MPH}$  flux are primarily concentrated in tropical countries, involving Africa, Central America, and Southeast Asia (Fig. 4A). On the other hand, the number of RKE flux outliers

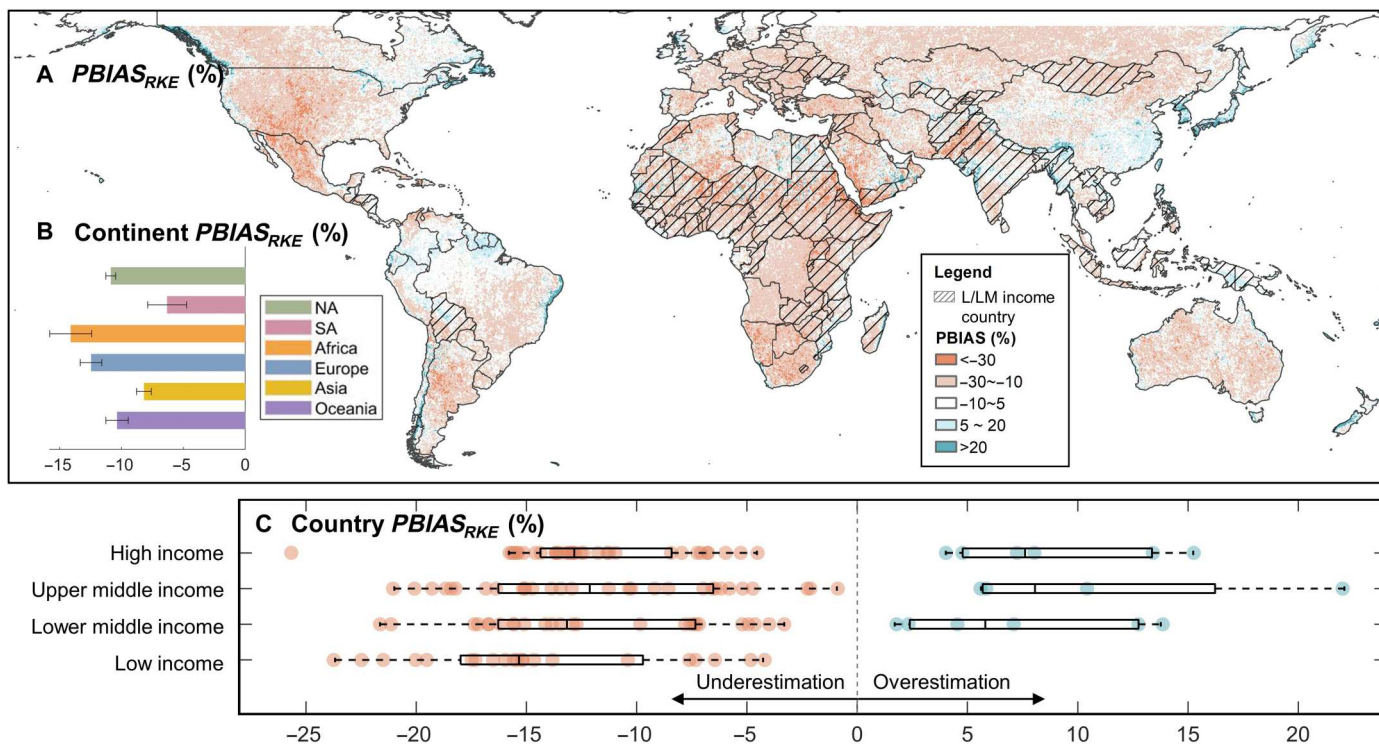


**Fig. 3. Summary statistics of the percent bias between  $RKE_{MPH}$  flux and  $RKE_{KE-I}$  flux ( $PBIAS_{RKE}$ ).** (A) The spatial pattern of the 5-year averaged  $PBIAS_{RKE}$  with low- and lower middle (L/LM)–GNI (Gross National Income) regions is highlighted with slashes. (B) Continental statistics of  $PBIAS_{RKE}$ . (C) The  $PBIAS_{RKE}$  boxplot of global countries classified into underestimating and overestimation groups with four income levels (high, upper middle, lower middle, and low). Note that the error bars in (B) represent interannual variations and the income classification was stated by the World Bank Analytical Classifications using GNI per capita in 2015 (43).

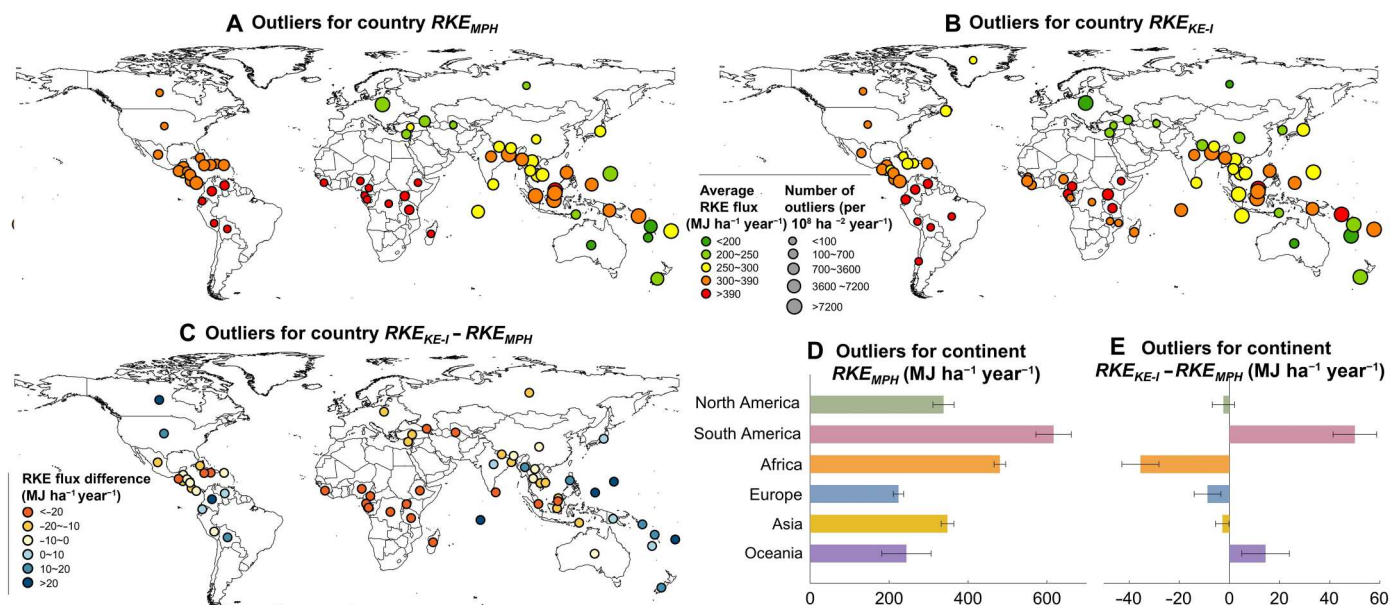


**Fig. 4. Summary of the outliers for RKE flux.** The magnitude and number of outliers for  $RKE_{MPH}$  flux (A) and  $RKE_{KE-I}$  flux (B) at the country level. (C) The difference in the averaged magnitude of outliers for  $RKE_{MPH}$  flux and  $RKE_{KE-I}$  flux. (D) Continental averaged magnitudes of outliers for  $RKE_{MPH}$ . (E) The difference in continental averaged outliers for  $RKE_{MPH}$  flux and  $RKE_{KE-I}$  flux, where the negative values show underestimation and positive values denote overestimation. Note that the outliers of European countries have been aggregated and the non-dot ones indicate the countries without any outlier. The error bars in (D) and (E) represent interannual variability.

Downloaded from https://www.science.org at University of Arizona on June 18, 2024

in the high-latitude countries, excluding European countries, is mostly less than  $100 \text{ per } 10^6 \text{ ha year}^{-1}$ . This number is much higher in the tropical countries, reaching  $7200 \text{ per } 10^6 \text{ ha year}^{-1}$ . We calculated the deviation between the high outliers for  $RKE_{MPH}$  flux and  $RKE_{KE-I}$  flux at the country level and found that most of the tropical countries, which can be considered as low-income countries, suffer from a large underestimation, with the difference reaching  $20 \text{ MJ ha}^{-1} \text{ year}^{-1}$  (Fig. 4C). The continental statistics also show that South America and Africa have the highest RKE flux outliers (Fig. 4D). However, extreme events for RKE flux show a large underestimation in Africa, while the ones in South America are largely overestimated (Fig. 4E). The extreme events of RKE flux (high outliers) may be the most critical factor in soil erosion assessment because the extreme rainfall can induce enormous soil mass wasting and landslides (12, 13).

### Widespread potential underestimation of rainfall erosivity using $KE-I$ relations

Last, we quantified rainfall erosivity based on  $RKE_{MPH}$  (fig. S12) and calculated the percent bias for the estimates of rainfall erosivity ( $PBIAS_R$ ) derived from  $RKE_{MPH}$  flux and  $RKE_{KE-I}$  flux (Fig. 5). Like what has been observed for RKE fluxes (Fig. 3), we found significant ( $P < 0.05$ ) potential underestimation of rainfall erosivity globally, with widespread negative  $PBIAS_R$  values (shown as warm color in Fig. 5A). The continental-level statistics also suggest that the largest underestimation of rainfall erosivity occurs in Africa, with an average  $PBIAS_R$  of  $\sim -8\%$  (Fig. 5B). We conducted the same country-level analysis for the  $PBIAS_R$  in the four income

levels. Results suggested that, in the underestimation group, the  $PBIAS_R$  in low-income countries are significantly ( $P < 0.05$ ) lower than in high-income countries, while the  $PBIAS_R$  among the other income levels do not show a significant difference ( $P > 0.05$ ) (Fig. 5C and fig. S13A). In the overestimation group, the  $PBIAS_R$  in low-income countries are significantly lower than that in all three levels ( $P < 0.05$ ) (Fig. 5C).

The deviations between  $RKE_{MPH}$  flux and  $RKE_{KE-I}$  flux and the associated rainfall erosivity are primarily due to the empirical nature of the equations, which relies largely on local ground observations. In this study, the empirical global  $KE-I$  relation used in RUSLE2 (for  $RKE_{KE-I}$ ) was established on the basis of the drop size data obtained from sites in agricultural landscapes in the United States, eastern Australia, and Zimbabwe, with a maritime climate condition (25–27). Except for the one used in RUSLE2, other empirical  $KE-I$  relations using the local observations were mostly obtained in high-income countries (8, 26, 28), such as the United Kingdom, the United States, and Australia, while the ones for low-income regions with different climates are still lacking (fig. S14). Thus, the extension of a universal  $KE-I$  relation to the global scale is questionable due to the variation of local climate and land cover (16) and may misguide the planning of regional water and land conservation, thus threatening the local food provisioning systems. Moreover, the existing  $KE-I$  relations developed using historical data may not be suitable for the rainfall microphysics with changes under global warming. This evidence enhances the necessity of using the radar-based RKE flux with better representation of rainfall microphysics characteristics for global rainfall erosivity estimation.

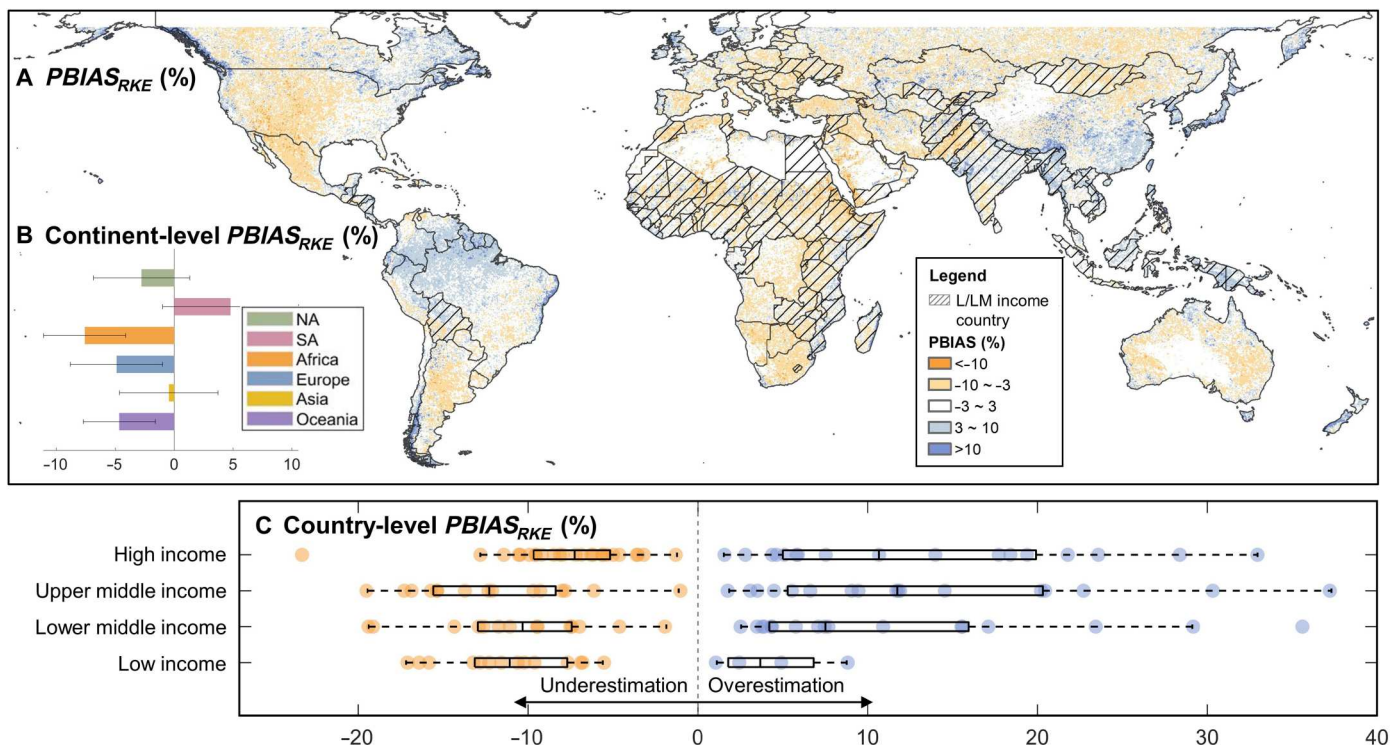


**Fig. 5. Comparison of rainfall erosivity estimates derived from  $RKE_{MPH}$  flux and  $RKE_{KE-I}$  flux.** (A) The spatial pattern of the 5-year averaged percent bias of rainfall erosivity ( $PBIAS_R$ ) estimates derived from  $RKE_{MPH}$  flux and  $RKE_{KE-I}$  flux with low-income regions is highlighted. (B) Continental statistics of the  $PBIAS_R$ . (C) The  $PBIAS_R$  boxplot of global countries classified into underestimating and overestimation groups with four income levels (high, upper middle, lower middle, and low). The error bars in (B) represent interannual variations.

## DISCUSSION

This study presents the development of raindrop microphysics using the latest radar measurements and a radar-based RKE estimation method. It is the first attempt to directly quantify  $RKE_{MPH}$  based on observed large-scale DSD for rainfall erosivity estimation, and our method has been validated in the United Kingdom (19, 20, 29) and China (30, 31) in previous studies. Our proposed method can effectively capture the spatial heterogeneity of RKE and rainfall erosivity. The application of rainfall microphysics products is one of the most promising technologies to fill the knowledge gaps of rainfall-related scientific problems. Considering the need for large-domain observation of rainfall erosivity, applications of radar measurements could be widely implemented in the near future (20).

RKE fluxes and the resulting rainfall erosivity are expected to increase under climate change. According to the ensemble climate projections of multiple climate models under different CO<sub>2</sub> emission scenarios defined by the Intergovernmental Panel on Climate Change (IPCC) (32), there would be a widespread increase in climate extremes with heavier rainfall (33), which would be most likely to increase the proportion of large raindrops (34) and further increase soil erosion. This is because weather systems feed on the water vapor stored in the atmosphere, and an increase in water vapor generally increases the intensity of precipitation. Furthermore, the phase change of water from snow and ice to liquid in clouds would increase the likelihood of precipitation falling as rain rather than snow (33). We therefore expect more rainfall in the future, which would result in substantial increase of RKE flux and rainfall erosivity. This fact potentially biases the existing  $KE-I$  relationship; therefore, direct inference of RKE from observations is more promising to capture the rainfall erosivity characteristics in the changing environment.

Although the accuracy of ground observations such as disdrometers is the most convincing, these observation-based sites are too few on a global scale (fig. S13). For example, the  $KE-I$  relations in the RUSLE2 model include three sites in the United States, two sites in Australia, and one site in Zimbabwe. Upscaling the empirical equation based on only six sites to the global scale would be problematic due to the obvious low representativeness of the climatic conditions and landscape features of the different sites, which has been also demonstrated by the recently updated  $KE-I$  relations worldwide (blue-colored sites in fig. S14). On the other hand, the limited number of observations inspires the approaches using remote sensing technology with more physical representations. Encouraged by the progress in this work, we argue that more coordinated efforts and investments are needed to improve the accuracy of global RKE estimates that are based on comprehensive rainfall microphysics. The combination of macroscopic and microscopic capabilities is promising to be improved by the scientific community to better constrain the associated parameters for a predictive understanding of soil erosion.

The substantial bias in the estimation of global RKE and the associated rainfall erosivity is primarily due to the uneven distribution of disdrometer observations, which are mostly located in limited sites with maritime climate conditions. Note that this study only highlights the spatial heterogeneity of RKE due to climate variation and does not imply a causal relationship between the underestimation of RKE and income levels. When climate conditions change, the performance of the fixed empirical equation may decrease

notably, as in the tropical African countries without disdrometer observations. These countries would be more challenged in the future to meet their growing food demand. The United Nations projects high population growth rates in these low-income countries, particularly in Africa, raising concerns about future food and water security (35). The projected expansion of cropland could substantially aggravate the devastating conditions that they now suffer. It also implies the weaker resilience responding to the increasing challenges in the future. Although the previous seminal research suggested that low-income countries experience higher rates of soil erosion (25), their estimates were still largely underestimated as revealed in this study. Better estimates are urgently needed in these regions to help decision-makers avoid the misleading results. The combination of skills is less dependent on the local equipment and thereby can help to mitigate the global knowledge inequalities.

## MATERIALS AND METHODS

We proposed a framework for  $RKE_{MPH}$  and the associated rainfall erosivity ( $R_{MPH}$ ) based on remote sensing data, including the DPR level-2A (2ADPR) product and the Integrated Multi-satellitE Retrievals for GPM (IMERG) product (fig. S1). The former radar data were used to generate the rainfall microphysical parameters using a gamma distribution function. The  $RKE_{MPH}$  was then estimated using the retrieval DSD and unit kinetic energy-generated method. The  $RKE_{MPH}$  was calibrated and validated using disdrometer data to ensure a solid performance of the RKE estimation. Last, the rainfall erosivity was calculated using the estimated RKE ( $RKE_{MPH}$ ) together with the rainfall intensity collected from the IMERG product (fig. S1). The detailed information on the generation of  $RKE_{MPH}$  and rainfall erosivity is given below.

### Gamma DSD function

The DSD, defined as the probability density function of raindrop size, is a statistical property that has been widely used to describe the microphysical characteristics of rainfall (35). We adopted a gamma distribution function to represent the natural DSD in the liquid phase using three geophysical parameters: mass-weighted mean raindrop diameter ( $D_m$ ), normalized intercept parameter ( $N_w$ ), and shape factor ( $\mu$ ). This function is commonly used to describe the natural variation of the DSD, given by the equation (36)

$$N(D) = N_w f(\mu) \left(\frac{D}{D_m}\right)^\mu \exp\left[-\frac{(4 + \mu)D}{D_m}\right] \quad (1)$$

$$f(\mu) = \frac{6(4 + \mu)^{\mu+4}}{4^4 \Gamma(\mu + 4)} \quad (2)$$

where  $\Gamma$  represents the gamma function,  $\mu$  is the shape factor of the gamma DSD,  $N_w$  (per millimeter per cubic meter) is the normalized intercept parameter, and  $D_m$  (millimeters) denotes the mass-weighted mean drop diameter. In the GPM DPR algorithm,  $\mu$  is assumed to be 3, so the two DPR-derived parameters ( $D_m$  and  $N_w$ ) are used to build the DSD model.

### DSD retrieval model using radar measurements

To derive the two unknown DSD parameters ( $D_m$  and  $N_w$ ), we obtained radar reflectivity at two different frequencies, where the

effective radar reflectivity factor can be expressed in terms of DSD and the backscattering cross section. In terms of radar waves, the Ku-band (13.6-GHz) and Ka-band (35.5-GHz) channels of the GPM DPR data occupy active phased array elements, providing high-resolution three-dimensional rain echoes. As rainfall intensity  $I_{DSD}$  can be estimated by the DSD model using

$$I_{DSD} = 6\pi \times 10^{-4} \int N(D)D^3 V(D)dD \quad (3)$$

where  $V(D)$  is the raindrop fall velocity related to the raindrop diameter. Then, two types of  $I$ - $D_m$  relationships are applied to the stratiform precipitation in Eq. 4 and to the convective precipitation in Eq. 5, as recommended by Iguchi *et al.* (37)

$$I_{DSD} = 0.401\epsilon^{4.649} D_m^{6.131} \quad (4)$$

$$I_{DSD} = 1.370\epsilon^{4.258} D_m^{5.420} \quad (5)$$

where  $\epsilon$  is an adjustment factor, and, once  $I_{DSD}$  and  $D_m$  have been determined,  $N_w$  can be obtained. Among the 176 sampling range bins in the vertical direction of the echo (each bin is ~125 m high), only bins above the ellipsoid have valid detections. We extracted 212, 329, and 561 pixel (or footprint) records in the surface real bin with ocean excluded from 2ADPR normal swath orbital Hierarchical Data Format version 5 (HDF5) files [ $49 \times 7926 \times 176 \times 32,537$  (number of beams in orbit width  $\times$  number of beams in orbit length  $\times$  number of spatial range bins  $\times$  number of orbital files)  $\approx 2.22 \times 10^{12}$  pixel records in total]. On the basis of the DSD parameters ( $D_m$  and  $N_w$ ) derived from each available DPR record, RKE can then be calculated by the corresponding pixel DSD model (20).

### Estimation of unit kinetic energy by DSD

In the proposed method, the unit kinetic energy is estimated from the mass and the terminal velocity of each raindrop, which was derived from the DSD with respect to the raindrop size and concentration. The raindrop kinetic energy ( $e$ ; unit, joules) shows strong relationships of increasing splash erosion with increasing energy, which is defined as follows

$$e = \frac{1}{2}mv^2 = \frac{1}{12}10^{-6}\pi\rho v^2 D^3 \quad (6)$$

where  $m$  (grams),  $v$  (meters per second), and  $D$  (millimeters) are the mass, terminal velocity, and diameter of a drop, respectively. The unit RKE ( $KE$ ) (joules per square meter per millimeter) for the  $t$ th minute can be calculated as the product of the kinetic energy of each drop of each diameter class  $k$ , as follows

$$KE_t = \frac{e_{sum}}{AP_t} = \frac{1}{AP_t} \sum_{k=1}^{mk} N_k e_k \quad (7)$$

where  $A$  represents the sample area (square meters),  $P_t$  is rainfall depth (millimeters) from  $(t - 1)$ th to  $t$ th minute, and  $N_k$  is the number of drops in class  $k$ . Because the kinetic energy of a drop is strongly related to its size and terminal velocity,  $e$  of a given drop is derived from the product of its mass and the square of its terminal velocity.

### RKE estimated using radar and $KE$ - $I$ relation

On the basis of the estimated unit RKE, the event RKE ( $E_e$ ) calculation is defined as

$$E_e = \sum_{t=1}^{nt} KE_t P_t \quad (8)$$

where  $P_t$  is the rainfall amount (millimeters) in the  $t$ th minute and  $nt$  is the number of time steps.

As mentioned above,  $KE$  for a specific location is determined on the basis of the size and velocity of the raindrops. However, because of the uneven distribution of ground disdrometers and the operational limitations of the satellite, the estimation of  $KE$  often relies on empirical relationships using rainfall intensity  $I_{IMERG}$  (millimeters per hour). The  $KE$ - $I$  relation widely used in the literature is expressed as an exponential relationship

$$KE = e_{max}(1 - ae^{-bl}) \quad (9)$$

where  $e_{max}$  is the maximum value of energy measured under high rainfall intensity and  $a$  and  $b$  are shape parameters. All of these parameters can be estimated by fitting curves using available DSD measurements. Here, the maximum  $KE$  can be determined by the parameters  $a$  and  $e_{max}$ , while the overall shape of the curve is modeled by the parameter  $b$ . The most commonly used  $KE$ - $I$  relation now is the following equation recommended by Brown and Foster (12) and revised in RUSLE2

$$KE = 0.29(1 - 0.72e^{-0.082I}) \quad (10)$$

However, the application of Eq. 10 has been mostly limited to the United States (38). On the basis of Eqs. 8 and 10, the global  $RKE_{MPH}$  and  $RKE_{KE-I}$  are estimated separately.

### RKE calibration

The estimation of  $RKE_{MPH}$  requires substantial calibration efforts. Here, we used DSD records to correct the estimates reproduced by the radar-derived RKE model. To ensure the data quality, we screened the raw data with the number of available DSD records exceeding 5 within a 30-min time interval. We quantified the arithmetic mean within the 5th to 95th percentile of the DPR-derived  $KE$  (RKE for the  $t$ th minute) records for a resistant measure. We georeferenced the record-based RKE and compared it to the grid-level RKE at a 30-min time scale. We aggregated the 30-min deviations to a daily level and performed adjustments for each grid based on the difference between the two RKEs.

We also conducted a bias correction on the final  $RKE_{MPH}$  product to mitigate the system errors of the radar observation. Here, ground disdrometers are considered as a reference for the correction of the RKE model driven by radar-derived  $KE$ - $I$  relations and IMERG rain rate data. We compared the mean RKEs generated by the two approaches at the daily level and conducted a first-order (linear, slope = 0.85 with intercept being set to be 0) adjustment for the entire RKE dataset.

### Rainfall erosivity estimation

Rainfall erosivity is commonly estimated by multiplying the accumulated RKE of the event by the maximum 30-min rainfall intensity ( $I_{30}$ ). We used a continuous 6-hour dry period interval (with no rainfall at all) to divide rainfall events (14, 24, 39) and predefined

the rainfall amount threshold as 12.7 mm to distinguish whether these events are erosive (14, 24). The start and end times of erosive rainfall events were recorded in all grids within 5 years.  $I_{30}$  can be approximated by rainfall intensity of 30-min equal intervals (40); therefore, we obtained event rainfall erosivity by multiplying event total RKE and event maximum rainfall intensity. We then calculated rainfall erosivity by summarizing event rainfall erosivity at monthly and annual scales.

### Validation

Uncertainty in the modeled results primarily originates from data measurement errors and the RKE derivation method. Therefore, we implemented a robust validation to ensure the quality of our RKE data product, including rainfall intensity validation and raindrop microphysics validation. For rainfall intensity data, we conducted validation using the National Oceanic and Atmospheric Administration Global Surface Summary of Day (41) meteorological data with 4,602,282 daily records spanning from 8557 available gauges during 2015–2019, 60°S to 60°N (see fig. S2). Moreover, for radar products, recent studies have suggested a notable improvement of the DSD obtained by DPR, especially because the technology is mature at the V06 stage (20, 39). Therefore, in this context, we used disdrometer data covering the period from 2015 to 2019 (which is consistent with the DPR operation time) as a reference for our DSD validation. We used Pearson's correlation coefficient and MAE to evaluate the DPR-derived formulas against the observed  $KE-I$  patterns. In addition, the mean values of rainfall microphysical parameters ( $D_m$  and  $N_w$ ) and the unit RKE ( $KE$ ) were compared between disdrometers and DPR at six intensity scenarios, including [0.1, 0.5], [0.5, 1], [1, 2], [2, 4], [4, 8], and  $\geq 8$  mm h<sup>-1</sup> in figs. S6 to S8.

### Statistical analyses

With  $RKE_{MPH}$  as the reference, we define  $PBIAS_{RKE}$  as

$$PBIAS_{RKE} = \frac{(RKE_{KE-I} - RKE_{MPH}) \times 100}{RKE_{MPH}} \quad (11)$$

Following the definition in Eq. 1, we quantified  $PBIAS_R$  as

$$PBIAS_R = \frac{(R_{KE-I} - R_{MPH}) \times 100}{R_{MPH}} \quad (12)$$

where  $R_{KE-I}$  and  $R_{MPH}$  represent rainfall erosivity derived from  $RKE_{KE-I}$  and  $RKE_{MPH}$ , respectively.

We quantified high outliers for the grid-scale RKE at the continental scale

$$\text{High outlier} = Q_3 + 1.5 \times IQR \quad (13)$$

where  $Q_3$  is third quartile and  $IQR$  is interquartile range.

We conducted linear regression for the country-level  $RKE_{MPH}$  and the associated rainfall erosivity (Figs. 3 to 5), setting  $P < 0.05$  as the statistical significance level. Countries with PBIAS less than 1% were removed from the linear regression. The 2015 cropland data shown in fig. S3 were obtained from History Database of the Global Environment land-use dataset (42), and GDP statistics for national and subnational analyses were obtained from the World Bank (43) and Kummu *et al.* (44), respectively.

### IMERG rainfall intensity data

IMERG-Final Run is a level 3 product of the GPM satellite that intercalibrates, merges, and interpolates with multiple satellite precipitation estimates while having part of the same data source as the DPR data that we used. It is a reliable precipitation data with high spatial ( $0.1^\circ \times 0.1^\circ$ ) and temporal (30-min) resolution and better performance (including correlation coefficient, bias, and errors) compared to other data fusion products (45, 46), such as CMORPH, TMPA 3B42RT, and TMPA 3B42V7.

### Supplementary Materials

This PDF file includes:

Supplementary Text

Figs. S1 to S15

Tables S1 to S3

References

### REFERENCES AND NOTES

1. FAO, ITPS, *Status of the World's Soil Resources (SWSR) – Main Report* (Food and Agriculture Organization of the United Nations and Intergovernmental Technical Panel on Soils, 2015).
2. A. Chappell, J. Baldock, J. Sanderman, The global significance of omitting soil erosion from soil organic carbon cycling schemes. *Nat. Clim. Change* **6**, 187–191 (2016).
3. E. Lugato, P. Smith, P. Borrelli, P. Panagos, C. Ballabio, A. Orgiazzi, O. Fernandez-Ugalde, L. Montanarella, A. Jones, Soil erosion is unlikely to drive a future carbon sink in Europe. *Sci. Adv.* **4**, eaau3523 (2018).
4. K. Van Oost, T. A. Quine, G. Govers, S. De Gryze, J. Six, J. W. Harden, J. C. Ritchie, G. W. McCarty, G. Heckrath, C. Kosmas, J. V. Giraldez, J. R. Marques Da Silva, R. Merckx, The impact of agricultural soil erosion on the global carbon cycle. *Science* **318**, 626–629 (2007).
5. L. Wang, Z. Shi, J. Wang, N. Fang, G. Wu, H. Zhang, Rainfall kinetic energy controlling erosion processes and sediment sorting on steep hillslopes: A case study of clay loam soil from the Loess Plateau, China. *J. Hydrol.* **512**, 168–176 (2014).
6. IPCC, *Climate Change and Land: An IPCC Special Report on Climate Change, Desertification, Land Degradation, Sustainable Land Management, Food Security, and Greenhouse Gas Fluxes in Terrestrial Ecosystems* (IPCC, 2019).
7. R. L. Fornis, H. R. Vermeulen, J. D. Nieuwenhuis, Kinetic energy–rainfall intensity relationship for central Cebu, Philippines for soil erosion studies. *J. Hydrol.* **300**, 20–32 (2005).
8. D. T. Meshesha, A. Tsunekawa, M. Tsubo, N. Haregeweyn, F. Tegegne, Evaluation of kinetic energy and erosivity potential of simulated rainfall using laser precipitation monitor. *Catena* **137**, 237–243 (2016).
9. D. Sempere-Torres, J. M. Porrà, J. D. Creutin, Experimental evidence of a general description for raindrop size distribution properties. *J. Geophys. Res. Atmos.* **103**, 1785–1797 (1998).
10. J. Nyssen, H. Vandenreyken, J. Poesen, J. Moeyersons, J. Deckers, M. Haile, C. Salles, G. Govers, Rainfall erosivity and variability in the Northern Ethiopian Highlands. *J. Hydrol.* **311**, 172–187 (2005).
11. C. E. Carter, J. Greer, H. Braud, J. Floyd, Raindrop characteristics in south central United States. *Trans. ASAE* **17**, 1033–1037 (1974).
12. L. Brown, G. Foster, Storm erosivity using idealized intensity distributions. *Trans. ASAE* **30**, 0379–0386 (1987).
13. P. Kinnell, Rainfall intensity-kinetic energy relationships for soil loss prediction. *Soil Sci. Soc. Am. J.* **45**, 153–155 (1981).
14. W. H. Wischmeier, D. D. Smith, *Predicting Rainfall Erosion Losses: A Guide to Conservation Planning* (Department of Agriculture, 1978).
15. P. Davison, M. G. Hutchins, S. G. Anthony, M. Betson, C. Johnson, E. I. Lord, The relationship between potentially erosive storm energy and daily rainfall quantity in England and Wales. *Sci. Total Environ.* **344**, 15–25 (2005).
16. V. Naipal, C. Reick, J. Pongratz, K. V. Oost, Improving the global applicability of the RUSLE model – Adjustment of the topographical and rainfall erosivity factors. *Geosci. Model Dev.* **8**, 2893–2913 (2015).
17. W. Berghuijs, R. Woods, M. Hrachowitz, A precipitation shift from snow towards rain leads to a decrease in streamflow. *Nat. Clim. Change* **4**, 583–586 (2014).
18. G. J. McCabe, D. M. Wolock, Long-term variability in Northern Hemisphere snow cover and associations with warmer winters. *Clim. Change* **99**, 141–153 (2010).
19. Q. Dai, J. Zhu, S. Zhang, S. Zhu, D. Han, G. Lv, Estimation of rainfall erosivity based on WRF-derived raindrop size distributions. *Hydrol. Earth Syst. Sci.* **24**, 5407–5422 (2020).

20. J. Zhu, S. Zhang, Q. Yang, Q. Shen, L. Zhuo, Q. Dai, Comparison of rainfall microphysics characteristics derived by numerical weather prediction modelling and dual-frequency precipitation radar. *Meteorol. Appl.* **28**, e2000 (2021).
21. E. A. Brandes, G. Zhang, J. Vivekanandan, An evaluation of a drop distribution-based polarimetric radar rainfall estimator. *J. Appl. Meteorol. Clim.* **42**, 652–660 (2003).
22. E. Adirosi, L. Baldini, A. Tokay, Rainfall and DSD parameters comparison between micro rain radar, two-dimensional video and parsivel2 disdrometers, and S-band dual-polarization radar. *J. Atmos. Ocean. Tech.* **37**, 621–640 (2020).
23. C. Prigent, Precipitation retrieval from space: An overview. *C. R. Geosci.* **342**, 380–389 (2010).
24. USDA-Agricultural Research Service, Science documentation: Revised universal soil loss equation, Version 2 (RUSLE 2) (USDA-Agricultural Research Service, Washington, DC, 2013); <https://www.ars.usda.gov/southeast-area/oxford-ms/national-sedimentation-laboratory/watershed-physical-processes-research/research/rusle2/revised-universal-soil-loss-equation-2-overview-of-rusle2/>.
25. P. Borrelli, D. A. Robinson, L. R. Fleischer, E. Lugato, C. Ballabio, C. Alewell, K. Meusburger, S. Modugno, B. Schütt, V. Ferro, V. Bagarello, K. Van Oost, L. Montanarella, P. Panagos, An assessment of the global impact of 21st century land use change on soil erosion. *Nat. Commun.* **8**, 2013 (2017).
26. A. Van Dijk, L. Bruijnzeel, C. Rosewell, Rainfall intensity–kinetic energy relationships: A critical literature appraisal. *J. Hydrol.* **261**, 1–23 (2002).
27. P. Panagos, P. Borrelli, J. Poesen, C. Ballabio, E. Lugato, K. Meusburger, L. Montanarella, C. Alewell, The new assessment of soil loss by water erosion in Europe. *Environ. Sci. Policy* **54**, 438–447 (2015).
28. M. Angulo-Martínez, S. Beguería, J. Kysely, Use of disdrometer data to evaluate the relationship of rainfall kinetic energy and intensity (KE-I). *Sci. Total Environ.* **568**, 83–94 (2016).
29. Q. Dai, Q. Yang, D. Han, M. A. Rico-Ramirez, S. Zhang, Adjustment of radar-gauge rainfall discrepancy due to raindrop drift and evaporation using the weather research and forecasting model and dual-polarization radar. *Water Resour. Res.* **55**, 9211–9233 (2019).
30. Q. Yang, Q. Dai, Y. Chen, S. Zhang, Y. Zhang, Effects of air pollution on rainfall microphysics over the Yangtze River delta. *J. Geophys. Res. Atmos.* **127**, e2021JD035934 (2022).
31. Q. Yang, Q. Dai, S. Zhang, K. Zhu, L. Zhang, Raindrop size distribution retrieval model for X-band dual-polarization radar in China incorporating various climatic and geographical elements. *IEEE Trans. Geosci. Remote. Sens.* **60**, 1–17 (2022).
32. IPCC, *Climate Change 2021: The Physical Science Basis. Contribution of Working Group I to the Sixth Assessment Report of the Intergovernmental Panel on Climate Change* (Cambridge University Press, 2021).
33. S. I. Seneviratne, X. Zhang, M. Adnan, W. Badi, C. Dereczynski, A. D. Luca, S. Ghosh, I. Iskandar, J. Kossin, S. Lewis, F. Otto, I. Pinto, M. Satoh, S. M. Vicente-Serrano, M. Wehner, B. Zhou, “Weather and climate extreme events in a changing climate,” in *Climate Change 2021: The Physical Science Basis. Contribution of Working Group I to the Sixth Assessment Report of the Intergovernmental Panel on Climate Change* (Cambridge University Press, 2021), chap. 11.
34. C. Caracciolo, F. Prodi, A. Battaglia, F. Porcu, Analysis of the moments and parameters of a gamma DSD to infer precipitation properties: A convective stratiform discrimination algorithm. *Atmos. Res.* **80**, 165–186 (2006).
35. FAO, *Africa Regional Overview of Food Security and Nutrition* (Food and Agriculture Organization of the United Nations and the United Nations Economic Commission for Africa, 2018).
36. Q. Dai, D. Han, Exploration of discrepancy between radar and gauge rainfall estimates derived by wind fields. *Water Resour. Res.* **50**, 8571–8588 (2014).
37. T. Iguchi, S. Seto, R. Meneghini, N. Yoshida, J. Awaka, M. Le, V. Chandrasekar, S. Brodzik, T. Kubota, *GPM/DPR Level-2 Algorithm Theoretical Basis Document (Version 6)* (NASA Goddard Space Flight Center, 2018).
38. P. Panagos, P. Borrelli, K. Meusburger, B. Yu, A. Klik, K. J. Lim, J. E. Yang, J. Ni, C. Miao, N. Chattopadhyay, S. H. Sadeghi, Z. Hazbavi, M. Zabihi, G. A. Larionov, S. F. Krasnov, A. V. Gorobets, Y. Levi, G. Erpul, C. Birkel, N. Hoyos, V. Naipal, P. T. S. Oliveira, C. A. Bonilla, M. Meddi, W. Nel, H. A. Dashti, M. Boni, N. Diodato, K. Van Oost, M. Nearing, C. Ballabio, Global rainfall erosivity assessment based on high-temporal resolution rainfall records. *Sci. Rep.* **7**, 4175 (2017).
39. M. Hanel, P. Máca, P. Bašta, R. Vlnas, P. Pech, The rainfall erosivity factor in the Czech Republic and its uncertainty. *Hydrol. Earth Syst. Sci.* **20**, 4307–4322 (2016).
40. S. Yin, Y. Xie, M. Nearing, C. Wang, Estimation of rainfall erosivity using 5- to 60-minute fixed-interval rainfall data from China. *Catena* **70**, 306–312 (2007).
41. NOAA National Centers for Environmental Information, *Global Surface Summary of the Day – GSOD* (2022); <https://ncei.noaa.gov/access/metadata/landing-page/bin/iso?id=gov.noaa.ncdc:C00516>.
42. K. K. Goldewijk, A. Beusen, J. Doelman, E. Stehfest, Anthropogenic land use estimates for the Holocene–HYDE 3.2. *Earth Syst. Sci. Data* **9**, 927–953 (2017).
43. World Bank, *World Bank Country and Lending Groups* (World Bank, 2022); <https://data.worldbank.org/indicator/NY.GNP.PCAP.CD>.
44. M. Kumm, M. Taka, J. H. Guillaume, Gridded global datasets for gross domestic product and Human Development Index over 1990–2015. *Sci. Data* **5**, 180004 (2018).
45. S. Jiang, L. Ren, C.-Y. Xu, B. Yong, F. Yuan, Y. Liu, X. Yang, X. Zeng, Statistical and hydrological evaluation of the latest Integrated Multi-satellite Retrievals for GPM (IMERG) over a midlatitude humid basin in South China. *Atmos. Res.* **214**, 418–429 (2018).
46. Z. Wang, R. Zhong, C. Lai, J. Chen, Evaluation of the GPM IMERG satellite-based precipitation products and the hydrological utility. *Atmos. Res.* **196**, 151–163 (2017).
47. B. S. Pickering, R. R. Neely III, D. Harrison, The Disdrometer Verification Network (DiVeN): A UK network of laser precipitation instruments. *Atmos. Meas. Tech.* **12**, 5845–5861 (2019).
48. C. Cerro, J. Bech, B. Codina, J. Lorente, Modeling rain erosivity using disdrometric techniques. *Soil Sci. Soc. Am. J.* **62**, 731–735 (1998).
49. M. A. Coutinho, P. P. Tomás, Characterization of raindrop size distributions at the Vale Formoso Experimental Erosion Center. *Catena* **25**, 187–197 (1995).
50. N. W. Hudson, Raindrop size distribution in high intensity storms. *Rhod. J. Agr. Res.* **1**, 6–11 (1963).
51. A. W. Jayawardena, R. B. Rezaur, Drop size distribution and kinetic energy load of rainstorms in Hong Kong. *Hydrol. Process.* **14**, 1069–1082 (2000).
52. Y. S. Lim, J. K. Kim, J. W. Kim, B. I. Park, M. S. Kim, Analysis of the relationship between the kinetic energy and intensity of rainfall in Daejeon, Korea. *Quat. Int.* **384**, 107–117 (2015).
53. J. S. Marshall, W. M. K. Palmer, The distribution of raindrops with size. *J. Atmos. Sci.* **5**, 165–166 (1948).
54. D. T. Meshesha, A. Tsunekawa, M. Tsubo, N. Haregeweyn, E. Adgo, Drop size distribution and kinetic energy load of rainfall events in the highlands of the Central Rift Valley, Ethiopia. *Hydrology. Sci. J.* **59**, 2203–2215 (2014).
55. D. T. Meshesha, A. Tsunekawa, M. Tsubo, N. Haregeweyn, E. Adgo, Evaluating spatial and temporal variations of rainfall erosivity, case of Central Rift Valley of Ethiopia. *Theor. Appl. Climatol.* **119**, 515–522 (2015).
56. K. Onaga, K. Shirai, A. Yoshinaga, S. E. Rimwanich, “Rainfall erosion and how to control its effects on farmland in Okinawa,” in *Land Conservation for Future Generations* (Department of Land Development, 1988), pp. 627–639.
57. H. S. Pedersen, B. Hasholt, Influence of wind speed on rainsplash erosion. *Catena* **24**, 39–54 (1995).
58. S. Petan, S. Rusjan, A. Vidmar, M. Mikoš, The rainfall kinetic energy–intensity relationship for rainfall erosivity estimation in the mediterranean part of Slovenia. *J. Hydrol.* **391**, 314–321 (2010).
59. C. J. Rosewell, Rainfall kinetic energy in eastern Australia. *J. Clim. Appl. Meteorol.* **25**, 1695–1701 (1986).
60. J. F. Sanchez-Moreno, C. M. Mannaerts, V. Jetten, M. Löffler-Mang, Rainfall kinetic energy–intensity and rainfall momentum–intensity relationships for Cape Verde. *J. Hydrol.* **454–455**, 131–140 (2012).
61. C. Zanchi, D. Torri, “Evaluation of rainfall energy in central Italy,” in *Assessment of Erosion* (Wiley, 1980), pp. 133–142.

#### Acknowledgments

**Funding:** This research was made possible partly by the National Natural Science Foundation of China (nos. 41871299, 42071364 and 42201020) and Fundamental Research Funds for the Central Universities and State Key Laboratory of Tropical Oceanography, CAS (LTO2325). **Author contributions:** Q.D., G.L., and Y.Y. initiated and designed this research. Q.D. presented and developed the model. Q.D. and J. Zhu implemented simulation experiments. All authors contributed to the writing and development of the manuscript. **Competing interests:** The authors declare that they have no competing interests. **Data and materials availability:** All data needed to evaluate the conclusions in the paper are present in the paper and/or the Supplementary Materials. The radar and IMERG data were obtained from the GPM Data Center archives web portal (available at <https://gpm.nasa.gov/data>). The relevant datasets of this study are archived for scientific and educational applications in National Earth System Science Data Center of China ([www.geodata.cn](http://www.geodata.cn)). Source data for Figs. 1 to 5 and figs. S1 to S15 are provided with the paper. Disdrometer data were sourced from the China Meteorological Administration, the Disdrometer Verification Network (DiVeN) in the United Kingdom (47), and GPM Ground Validation mission (<https://ghrc.nsstc.nasa.gov/home>). Other relevant data for model are available at the box site of Auburn University (<https://auburn.box.com/v/Rainfallkineticenergy>).

Submitted 5 January 2023

Accepted 6 July 2023

Published 9 August 2023

10.1126/sciadv.adg5551